Planetary and Space Science xxx (xxxx) xxx–xxx

Contents lists available at ScienceDirect

Planetary and Space Science

journal homepage: www.elsevier.com/locate/pss

Numerical prediction of meteoric infrasound signatures

Marian Nemec[a,*], Michael J. Aftosmis[a], Peter G. Brown[b]

[a] Advanced Supercomputing Division, NASA Ames Research Center, USA
[b] Department of Physics and Astronomy, University of Western Ontario, Canada

ARTICLE INFO

Keywords:
Meteoroid
Shock wave
Infrasound
Simulation
Numerical modeling

ABSTRACT

We present a thorough validation of a computational approach to predict infrasonic signatures of centimeter-sized meteoroids. This is the first direct comparison of computational results with well-calibrated observations that include trajectories, optical masses and ground pressure signatures. We assume that the energy deposition along the meteor trail is dominated by atmospheric drag and simulate a steady, inviscid flow of air in thermochemical equilibrium to compute a near-body pressure signature of the meteoroid. This signature is then propagated through a stratified and windy atmosphere to the ground using a methodology from aircraft sonic-boom analysis. The results show that when the source of the signature is the cylindrical Mach-cone, the simulations closely match the observations. The prediction of the shock rise-time, the zero-peak amplitude of the waveform and the duration of the positive pressure phase are consistently within 10% of the measurements. Uncertainty in primarily the shape of the meteoroid results in a poorer prediction of the trailing part of the waveform. Overall, our results independently verify energy deposition estimates deduced from optical observations.

1. Introduction

The hypersonic entry of meteoroids into the atmosphere generates strong shock waves that decay as they propagate to the ground. Delayed sounds from meteors have been known since ancient times. Systematic investigations of meteoric pressure disturbances began in the early part of the 20th century, even being proposed as an early form of atmospheric temperature probing (Whipple, 1923). Nowadays, pressure signatures recorded by dedicated sensor arrays are being actively investigated to explain various aspects of meteoroid entry, impact and origin (Evers and Haak, 2001; Liszka, 2008; Edwards, 2009).

Along with observational capabilities, analytic models of meteor-generated pressure waves were developed in the Soviet Union (Tsikulin, 1970) and in the United States (ReVelle, 1974, 1976). These models provide a simple prediction of the period and maximum amplitude of the wave when it reaches the ground. Near the trajectory, the strong bow shock of the meteoroid is modeled as a cylindrical blast wave that decays into a weak shock called an N-wave. The attenuation of the N-wave as it propagates through the atmosphere is approximated using weak-shock theory and, as the effects of nonlinearity diminish, linear wave theory. ReVelle (1974, 1976) derived closed-form expressions for the period and maximum amplitude from relations involving the blast-wave radius, geometrical acoustics and empirical correlations based on studies of lightning discharges (Jones et al., 1968; Few, 1969).

The analytic models indicate that the detection of meteoric infrasound[1] should be fairly common – especially infrasound from small regional events where the wave propagation distance through the atmosphere is relatively short. Until recently, however, few such measurements existed (Edwards, 2009). Consequently, the models have not been properly validated despite being widely employed in both the infrasound and meteor communities to estimate energy deposition (ReVelle and Whitaker, 1999; Brown et al., 2007).

To address this issue, a long-term campaign of simultaneous optical and infrasound measurements began in 2006 in Canada with the goal of producing a well-constrained meteor dataset that includes orbital parameters, light curves and trajectory parameters, and pressure signatures (Edwards et al., 2008; Silber and Brown, 2014). The instrumentation involves an optical network of 7–14 all-sky camera stations that detects and astrometrically measures meteors (Weryk et al., 2008). The pressure signatures are recorded at the Elginfield Infrasound Array (ELFO), which is a four-sensor microbarograph array located near the geographical center of the optical network. Observations through the end of 2011 captured 71 events (Silber and Brown, 2014). These were analyzed by Silber et al. (2015), who found that the analytic model of ReVelle (1976) produces reasonable agreement with optical observations when the meteoroid's blast radius is estimated

* Corresponding author.
E-mail addresses: marian.nemec@nasa.gov (M. Nemec), michael.aftosmis@nasa.gov (M.J. Aftosmis), pbrown@uwo.ca (P.G. Brown).

[1] Inaudible, low-frequency (<20 Hz) pressure waves.

http://dx.doi.org/10.1016/j.pss.2017.03.003
Received 1 December 2016; Received in revised form 18 February 2017; Accepted 6 March 2017

from period measurements. Comparisons based on amplitude measurements, however, show a large mismatch, hinting at shortcomings of the ReVelle (1976) model that Silber et al. (2015) attribute chiefly to the choice of the transition altitude from the weakly-nonlinear to the linear regime.

To improve the prediction of the ground waveform, Haynes and Millet (2013) modify the ReVelle (1976) model by implementing the F-function approach of Whitham (1956) for the propagation of weak shocks. This relaxes the requirement of explicitly specifying the transition altitude. Henneton et al. (2015) explore a numerical approach that is much more general. They use computational fluid dynamics to determine the near-body flow around the meteoroid, extract a nearfield pressure signature, and then propagate this signature to the ground by solving the augmented Burgers' equation to accurately model atmospheric absorption. Their numerical experiments agree well with the ReVelle (1976) model in the asymptotic limits of infinite meteoroid velocity and vanishing size. Both Haynes and Millet (2013) and Henneton et al. (2015), however, test their simulations by reproducing the signature from the Carancas fireball-crater event, where details of the trajectory, energy and dynamics are very uncertain (Brown et al., 2008; Le Pichon et al., 2008).

In this work, we investigate a computational approach similar to that of Henneton et al. (2015), which we adapt from our work in simulation-based aircraft sonic-boom prediction (Aftosmis and Nemec, 2014). We use the new, homogenous dataset of Silber et al. (2015) to test our simulations. This dataset provides significantly better validation benchmarks than the Carancas event used in previous studies. The entry of the Stardust capsule (Plotkin et al., 2006; Revelle and Edwards, 2007), which is a convenient “artificial” meteor, is used for initial validation. Thereafter, we consider four well-constrained meteor events from Silber et al. (2015) and assess the ability of the computational approach to reproduce the observed travel times and waveforms.

More broadly, we demonstrate the potential of using high-fidelity simulations to interpret meteor observations. Our approach is especially valuable as an independent estimate of energy deposition for meteoroids that generate observable ground-pressure signatures. Ignoring deceleration, the mass loss $\mathrm{d}m$ over the trail length $\mathrm{d}\ell$ of a meteoroid generating the observed signature is given by

$$\frac{\mathrm{d}m}{\mathrm{d}\ell} = \frac{2}{v^2}\frac{\mathrm{d}E}{\mathrm{d}\ell} \tag{1}$$

where v is the velocity of the meteoroid and $\mathrm{d}E/\mathrm{d}\ell$ the energy deposition per unit trail length. Unlike previous analyses (Edwards, 2009; Silber et al., 2015) that rely on the concept of blast radius to estimate $\mathrm{d}E/\mathrm{d}\ell$, we show that high-fidelity nearfield simulations, such as those of Henneton et al. (2015) and Aftosmis et al. (2016), can be used to estimate energy deposition directly. Consequently, these simulations offer a promising path to a better understanding of the near-body shock system at the source point along the meteoroid's trajectory that generates the observed signature. Furthermore, accurate prediction of pressure signatures may help in calibrating, or anchoring, optical and radar observations, as well as improve the reconstruction of meteor events from solely infrasound observations.

2. Problem setup and numerical method

Fig. 1 shows a sketch of the physical domain with a meteoroid entering the atmosphere and generating a strong, detached shock wave. Our goal is to determine the ground pressure signature. We assume that the energy deposition $\mathrm{d}E/\mathrm{d}\ell$ in Eq. (1) is wholly from the atmospheric drag force. This neglects energy loss due to radiation, but this component typically does not exceed 5% of the total (Ceplecha et al., 1998; Ceplecha and ReVelle, 2005). A representative case is a small meteoroid with a characteristic diameter, D, not exceeding a few centimeters entering the upper atmosphere at a hypersonic speed of around 20 km/s. As shown in Fig. 1, the meteoroid's Mach cone is

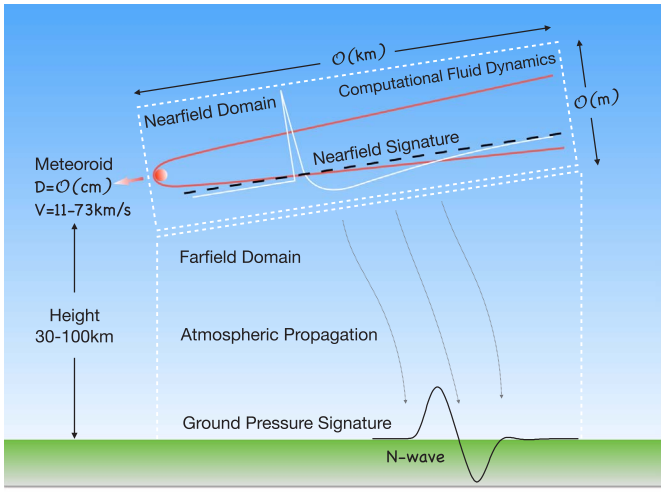

Fig. 1. Sketch of meteoroid entry generating a strong, cylindrical, blast-like pressure pulse that attenuates as it propagates to ground.

essentially cylindrical, which is a consequence of the small Mach angle (<2°) due to the high entry speed.

Following the approach of Tsikulin (1970) and ReVelle (1974, 1976), the physical domain is divided into a cylindrical nearfield region surrounding the trajectory and a farfield region, as illustrated in Fig. 1. In the nearfield, close to the body, the flow is three-dimensional, strongly nonlinear, and dominated by complex physical processes that include real-gas effects, ablation, and often fragmentation. The use of computational fluid dynamics in this region avoids many of the simplifying assumptions that limit the accuracy of blast-wave theory, but presumes some knowledge of the energy deposition. As the bow shock propagates outward, the radial extent of the nearfield must be large enough to allow the shock to weaken sufficiently and the flow to become locally axisymmetric. The problem in the farfield can then be treated as a quasi-one-dimensional propagation of an acoustic waveform. Fig. 1 shows a typical, blast-like, nearfield signature (white line) that is extracted several body lengths below the trajectory of the meteoroid, along the black dashed line.

The ideas of splitting the physical domain and using a numerical simulation in the nearfield to initialize an atmospheric propagation in the farfield are well established in the field of aircraft sonic-boom analysis (Whitham, 1956; Cheung et al., 1990; Siclari and Darden, 1991; Page and Plotkin, 1991; Maglieri et al., 2014). Moreover, simulation-based sonic-boom prediction has been thoroughly validated (Park et al., 2013; Park and Morgenstern, 2016) and is being applied regularly in the design of low-boom aircraft prototypes (Haering et al., 2005; Wintzer et al., 2015). In principle, it is straightforward to apply the computational approach of sonic-boom analysis to the prediction of meteoric pressure signatures. In practice, however, the challenges of hypersonic flow, longer and higher altitude atmospheric propagation, and weaker and lower-frequency signatures require special attention. In the next two subsections, we provide details of the nearfield and farfield solvers that specifically address these challenges.

2.1. Nearfield domain

In the nearfield, we specify a uniform atmosphere and solve the steady, three-dimensional Euler equations governing the compressible flow of air in thermochemical equilibrium. Assuming negligible ablation and a continuous medium, this inviscid flow model should predict nearfield signatures accurately for single-body meteoroids, except for the influence of viscous effects from the wake region. While not negligible, the pressure fluctuations in the wake due to viscous effects should be small relative to the large overpressure of the detached bow shock that dominates the signature.

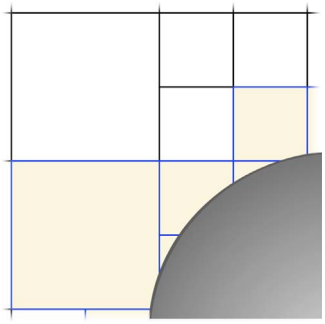

Fig. 2. A multilevel Cartesian mesh with a cut-cell boundary.

For a finite region of space with volume V and surface area A, the integral form of the Euler equations is given by

$$\frac{\mathrm{d}}{\mathrm{d}t}\int_V \mathbf{Q}\,\mathrm{d}V + \oint_A \mathbf{F}\cdot\hat{\mathbf{n}}\,\mathrm{d}A = 0 \tag{2}$$

where $\mathbf{Q} = [\rho, \rho u, \rho v, \rho w, \rho E]^{\mathrm{T}}$ is the vector of conserved state variables including the density ρ, the Cartesian momentum components, ρu, ρv and ρw, and the total energy per unit mass, E; $\mathbf{F}$ is the inviscid flux tensor; and $\hat{\mathbf{n}}$ is the outward facing unit normal. The thermodynamic properties of air, namely pressure, sound speed and temperature, are obtained from curve fits of tabulated data from the work of Srinivasan et al. (1987) since the perfect gas equation of state is not appropriate at meteoroid entry conditions.

The Euler equations are solved with a finite-volume method on a Cartesian mesh with embedded boundaries (Aftosmis et al., 1998, 2000). The volume mesh consists of hexahedral cells, except for a layer of cut cells, which are cells clipped into arbitrarily shaped polyhedra by the meteoroid's surface, as illustrated in Fig. 2. The meteoroid geometry is specified by a watertight surface triangulation. The spatial discretization uses a cell-centered, second-order accurate, finite-volume method with a weak imposition of boundary conditions. Steady-state solutions are obtained using a five-stage Runge–Kutta scheme accelerated by local time stepping, multigrid and parallel computing (Berger et al., 2005a, 2005b).

To set the radius at which the signature is extracted, we follow the work of ReVelle (1974, 1976) and Henneton et al. (2015), and use the blast radius of a cylindrical line source as a guide. The blast radius represents the distance from the body at which the shock overpressure ratio falls below unity, $\Delta p/p_\infty < 1$, where p_∞ is the freestream (undisturbed ambient) pressure. Strong-shock overpressures have $\Delta p/p_\infty > 10$, so at a relaxation distance of one blast radius the pressure signature will be well outside the region of strongly nonlinear shocks. When energy deposition is dominated by drag, a simple approximation of the blast radius is the product $M_\infty D$, where M_∞ is the meteoroid's freestream Mach number and D the diameter. While this condition is not rigorous, we find minimal variation in the propagated waveforms when the nearfield signatures are extracted at or beyond this distance. Moreover, for meteoroid sizes of a few centimeters the blast radius is on the order of a few meters to tens of meters. This is much smaller than the atmospheric scale height, which justifies the use of a uniform atmosphere in the nearfield.

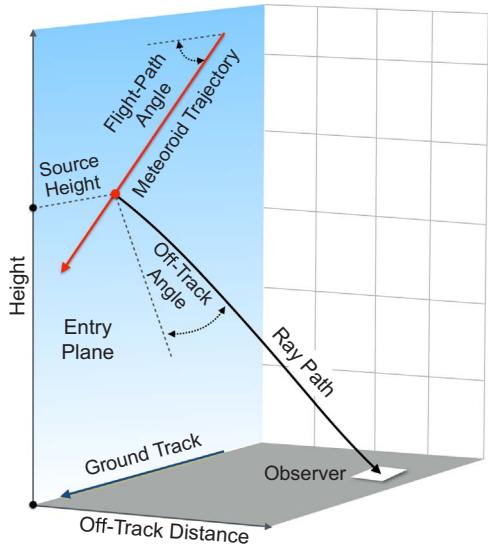

Fig. 3. Ray path from a source point on the trajectory to the observer.

The primary challenge of the nearfield simulation is the highly anisotropic flowfield. To explain, consider a spherical meteoroid with diameter $D = 1$ cm and $M_\infty = 50$. At these conditions, the blast radius is 50 cm, or 50 body-lengths, and the Mach angle is 1.1°. This means that the bow shock will reach the extraction location of the nearfield signature approximately 26 m downstream from the meteoroid, or 2600 body-lengths. Moreover, as sketched in Fig. 1, the computational domain must continue well downstream of the leading shock to capture the over-expansion and recompression of the blast wave. This leads to computational domains that are on the order of meters in the crossflow (transverse) direction, but may span kilometers in the streamwise direction, while needing to resolve a meteoroid only a few centimeters in diameter.

We address this wide range of scales through use of adaptive mesh refinement based on the method of adjoint-weighted residuals (Nemec and Aftosmis, 2014). The strength of this method is its ability to refine only those cells of the computational domain that most affect the numerical accuracy[2] of the nearfield signature. To give a rough idea of computational cost, the simulations presented in this work use meshes with approximately 100 million cells. These problems require approximately 24 h to mesh, adapt and solve on a computer with 28 cores.[3]

2.2. Farfield domain

The nearfield signature is propagated through the atmosphere via a two-step procedure. The first step involves ray tracing to compute the path of the signature from the meteoroid trajectory to the location of the microphone array. The second step involves determining the shape of the signature as it travels along this ray path. We use the sBOOM code by Rallabhandi (2011) for both steps of the propagation.

Fig. 3 shows an example ray path from the meteoroid to the observer. The path is generally curved due to the effects of atmospheric stratification and wind. The launch direction of the ray is normal to the meteoroid's cylindrical Mach-cone consistent with our assumption of energy deposition being dominated by the drag of a single-body meteoroid.[4] The range for the off-track angle is constrained between −90° and 90°, depending on the location of the observer. As indicated in Fig. 3, this means that only "direct arrivals" are considered. These are signatures along ray paths that are initially cast in a downward direction from the trajectory. Secondary paths due to refraction in the upper atmosphere are neglected because these are generally much weaker. This limits the wave propagation distance to about 300 km, thereby limiting atmospheric variabilities that arise in long-range propagation, e.g. at distances of 1000s of kilometers.

For a given flight path angle, observer location, atmospheric conditions and measured travel time, we search for the unique source height with a direct ray path from the trajectory to the observer. The ray tracing proceeds by marching down the trajectory and finding an off-track angle for which the ray-path ground intercept is within some

[2] The level of discretization error due to cell-size.

[3] Intel Xeon E5-2680v4 (Broadwell) processors.

[4] Actual observations (Brown et al., 2007) show that the launch angle can deviate by as much as 20° from the normal.

small radius of the observer (typically one kilometer). The travel-time residual between the computed and observed values is monitored and the source height is adjusted until the residual is minimized. This establishes the travel time of the signature to within a few seconds.

If a ray path is not found, Silber et al. (2015) suggest that this is an indication that the observed signature does not originate from the cylindrical Mach-cone, but is instead from a more omnidirectional shock front, such as a quasi-spherical wave, that may arise during the disintegration of the meteoroid. To test this, Silber et al. (2015) perturb the ray launch direction away from the Mach-cone normal and look for viable ray paths. We use a similar procedure that involves artificially perturbing the flight path angle to affect the ray launch direction. This is especially useful when dealing with observations of multiple signatures from the same trajectory. The ray-tracing procedure allows us to identify which signature is most likely from the cylindrical Mach-cone generated by the meteoroid's ballistic flight.

The evolution of the waveform as it descends to the ground is modeled through use of the augmented Burgers' equation (Cleveland, 1995; Millet and Haynes, 2010; Rallabhandi, 2011; Yamamoto et al., 2015). In dimensionless form, the equation is given by

$$\frac{\partial p}{\partial \sigma} = p\frac{\partial p}{\partial \tau} + \frac{1}{\Gamma}\frac{\partial^2 p}{\partial \tau^2} + \sum_{\nu} C_\nu \left(1 + \theta_\nu \frac{\partial}{\partial \tau}\right)^{-1} \frac{\partial^2 p}{\partial \tau^2} - \frac{p}{2S}\frac{\partial S}{\partial \sigma} + \frac{p}{\rho_0 c_0}\frac{\partial(\rho_0 c_0)}{\partial \sigma} \tag{3}$$

where p is pressure, σ the distance, τ the time, C_ν the dispersion parameter, Γ the thermoviscous parameter, θ_ν the molecular-relaxation time parameter of the νth relaxation process, and ρ_0 and c_0 the local density and speed of sound, respectively, and S the ray tube area of adjacent ray paths. The equation is solved in the time domain using operator splitting and a finite-difference discretization (Rallabhandi, 2011).

By including classical and molecular-relaxation losses, in addition to the stratification, spreading and nonlinear terms, the solution of the augmented Burgers' equation directly predicts shock rise time.[5] This is important because the rise time determines the frequency spectrum of the signature. Moreover, Silber et al. (2015) report large differences in maximum amplitude when comparing their observations to predictions based on an improved version of the ReVelle (1976) model. The general formulation of the augmented Burgers' equation provides a potentially more accurate approach. We note that the absorption coefficients of Sutherland and Bass (2004) are not used, but this should not be a significant source of error since the source heights for the selected cases are all below 80 km.

3. Method validation – Stardust entry

We simulate the entry of the Stardust capsule to establish the accuracy of our computational approach on a highly constrained case. As part of its mission to collect dust particles, Stardust closely matched the orbit of comet 81P/Wild-2. Consequently, its atmospheric entry mimicked that of a cometary meteoroid, and with a speed of 12.8 km/s, it remains one of the fastest entries of a man-made object. Crucially, unlike meteoroids, the capsule shape is known precisely, see for example Stackpoole et al. (2008). Moreover, the capsule's ballistic trajectory, pressure signature, and the atmospheric conditions are well documented (Plotkin et al., 2006; Revelle and Edwards, 2007; Desai and Qualls, 2008; Trumble et al., 2010) and its energy deposition is designed to be dominated by drag.

We test our computational approach by trying to reproduce the pressure measurements of Plotkin et al. (2006), who used B&K 4193 low-frequency microphones digitized at 24 kHz to record a signature very close to the capsule's ground track. The entry occurred on 15 January 2006. The capsule shape was a 60° half-angle spherically-blunted cone with a diameter $D = 0.81$ m. The capsule reached the signature's source height, H, of 50.4 km at 09:57:49.078 UTC, by which point the capsule had decelerated to 6.4 km/s. This corresponds to a freestream Mach number of 19.4. The capsule's flight-path angle was constant at 8.2° and its deceleration at the source height was 0.18 km/s^2.

Fig. 4 shows the computed pressure field near the capsule. The flow is dominated by a detached bow shock, a thin shock layer and weaker wake shocks that merge downstream. The blast radius of the capsule is 15.7 m, or 19.4D, at the source height. Fig. 5 shows the nearfield signature extracted streamwise at a distance of 20D below the capsule, or slightly over one blast radius away. The time (in milliseconds) on the x-axis is obtained by normalizing the distance along the sensor by the speed of the capsule. Observe that the shock overpressure ratio is well less than 1, which indicates that the main shock is approaching the weakly nonlinear regime. Moreover, while the amplitude of the signature is dominated by the shock, its duration is dominated by the over-expansion and the slow recompression.

To propagate the nearfield signature to the ground, we use the recorded temperature and wind profiles from Desai and Qualls (2008) and a relative humidity profile based on the U.S. Standard Atmosphere (1976). Ray tracing reveals that due to the unusually strong winds that night, the ray launch direction is at an off-track angle of 4° even though the microphone array is located essentially on-track. Fig. 6 shows the attenuation and lengthening of the signature as it propagates through the atmosphere. The signature labeled “Nearfield” is the waveform after just 100 m of propagation, which is very similar to the one shown in Fig. 5, except here we plot overpressure instead of overpressure ratio.

After about 1 km of propagation (red signature at height of 49 km in Fig. 6), the peak has attenuated significantly and there is already a small increase in the duration of the positive pressure phase. After 10 km of propagation (green signature at height of 40 km), the signature is a classic N-wave and the time to the zero-crossing has more than doubled. Counterintuitively, the amplitude thereafter increases with propagation distance. This is simply due to the exponentially increasing ambient pressure as the signature descends and should not be confused with the overpressure *ratio*, which always decreases. Over the last 20 km of propagation, there are essentially no changes in the duration of the positive pressure phase or the overall period. This indicates that the wave has reached the linear regime.

Fig. 7 compares the computed ground signature with the measurements of Plotkin et al. (2006). Data from three microphones is shown, labeled “Channel 2” through “4”. Overall, the agreement is excellent, especially in terms of the shock rise time and the duration of positive pressure phase. The maximum amplitude is overpredicted by about 10%. This can be attributed to the rapidly changing atmospheric conditions due to unusual blizzard conditions in the region of the microphone array, as well as to using the as-built capsule geometry in the simulation instead of the ablated shape.[6] The largest differences occur during the negative pressure phase. The expansion in the measured signature is not as deep and the recompression to ambient pressure is much more gradual. These differences may be partially attributed to the modeling fidelity of the nearfield wake region in addition to the uncertainty in the atmospheric conditions. Nevertheless, there is good agreement in the signal period. Lastly, Plotkin et al. (2006) report a travel time of 161 s for the signature to reach the microphones and we compute a travel time of 162.2 s. The agreement is excellent; the computation is within 1% of the observed value, which is well within the uncertainty of the atmospheric model.

4. Meteor events

We select four meteor events from the Silber et al. (2015) dataset. Our primary selection criterion is a limit on the source height – we

[5] Shock rise time is the time between the onset and first overpressure peak in the signature.

[6] We note that the recession depth was only a few millimeters, so the shape change due to ablation should not significantly affect the signature (Stackpoole et al., 2008).

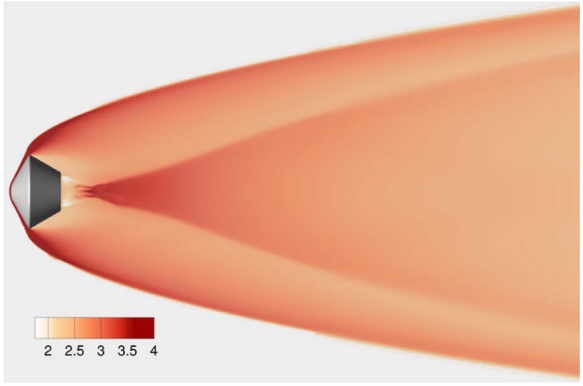

Fig. 4. Pressure contours around the Stardust capsule ($\log_{10}p$, $M_\infty = 19.4$, $H = 50.4$ km, $p_\infty = 72.2$ Pa, $D = 0.81$ m, equilibrium air model).

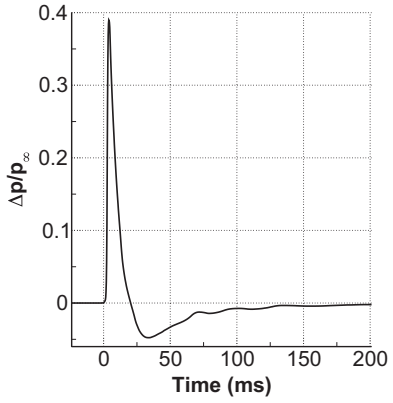

Fig. 5. Pressure signature at distance of $20D$, $M_\infty = 19.4$, $H = 50.4$ km.

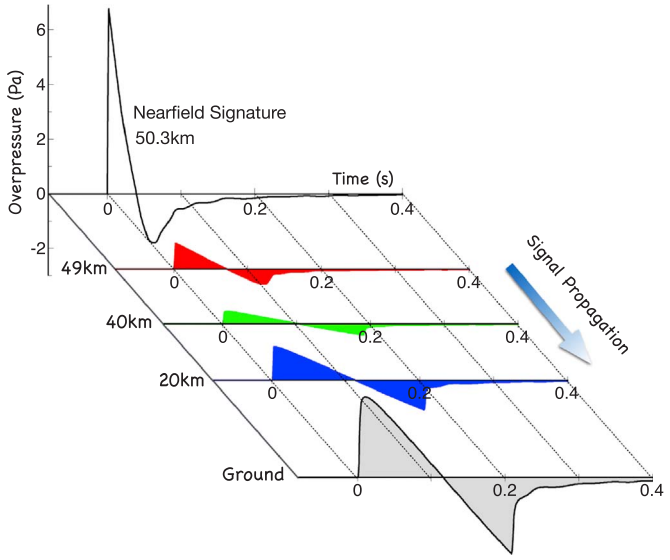

Fig. 6. Evolution of the Stardust signature as it propagates to the ground through a stratified, windy atmosphere (constant ground reflection factor). (For interpretation of the references to color in this figure, the reader is referred to the web version of this article).

consider only events for which the source height does not significantly exceed 70 km. For centimeter-sized meteoroids this is on the boundary between the continuum and the transitional regime (Kn ≈ 0.1), since the mean free path at 70 km is approximately 1 mm. We also check each meteor's light curve (Silber, 2014) and pick events for which the source height does not coincide with major peaks in the light curve. These correspond to flares that are usually associated with meteoroid fragmentation. Thorough analysis of pressure signatures from such events is beyond the scope of this work.

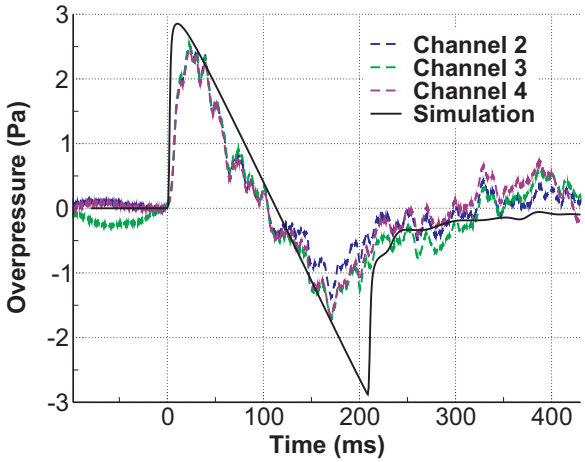

Fig. 7. Observed and computed ground pressure signatures for the Stardust capsule.

Table 1
A summary of entry parameters for the selected meteor events from Silber et al. (2015).

Date	Entry Speed[a] (km/s)	Begin Height (km)	End Height (km)	Flight Path Angle[b] (deg.)	Entry Mass[c] (g)
20080325	13.5	76.2	32.8	44.8°	917
20081028	15.8	81.2	41.1	33.1°	110
20090428	21.2	83.5	38.0	57.2°	330
20111005	29.1	96.2	64.5	46.8°	20

[a] Meteoroid speed at the onset of ablation.
[b] Measured from horizontal in the plane of entry, see Fig. 3.
[c] Mass based on the FM model of Ceplecha and ReVelle (2005).

Table 1 summarizes the entry parameters of the selected meteors. Note that a flight path angle of 90° represents a vertical entry and that the flight path angle is assumed to be constant along the trajectory. Table 2 shows the source heights of the signatures for the selected cases as determined by Silber et al. (2015). Note that Meteor 20090428 features two arrivals. The column labeled "Total Range" is the distance between the ELFO infrasound array and the source point on the trajectory. Hence, ELFO is 70–150 km away from the source points and the signatures take 4–8 min to travel there. Overall, the selected cases provide a broad overview of signatures typical of many events.

5. Results

5.1. Source height and travel time

To establish the freestream conditions of the nearfield simulations, we independently verify the source heights listed in Table 2. We use these source heights as initial conditions and seek to find an off-track angle for which the ray path intercepts the ground within a kilometer of ELFO's central element. This tolerance is based on ELFO's aperture, which is approximately 600 m. Our atmospheric conditions, namely temperature and wind, are identical to those used by Silber et al. (2015).[7]

Table 3 summarizes the ray tracing results. The middle three columns give the computed source height and the ray launch direction that result in ray paths with small travel-time residuals. Note that column 4, labeled "ΔFPA", tracks changes in the flight path angle.

[7] The mean atmospheric conditions for each event are defined by a spline fit between the United Kingdom Meteorological Office (UKMO) wind model (Swinbank and O'Neill, 1994) below 60km and the HWM95 (Hedin et al., 1996) and NRL-MSIS00 models (Picone et al., 2002) at high altitude.

Table 2
A summary of signature source heights and travel times (Silber et al., 2015).

Date	Source Height (km)	Total Range[a] (km)	Travel Time (s)
20080325	61.6 ± 0.6	113.1	341
20081028	52.7 ± 3.6	73.3	240
20090428	60.7 ± 6.2	138.6	456
20090428	70.9 ± 1.1	140.6	460
20111005	77.8 ± 4.2	131.3	407

[a] Distance from observatory to the source-height point on the trajectory.

Table 3
Computed source heights and travel times.

Date	Source Height (km)	Off-track Angle (deg.)	ΔFPA[a] (deg.)	Travel Time (s)	% Diff
20080325	61	50°	−16.8°	341.1	0.03
20081028	53.7	36.5°	0	236	−1.7
20090428	58.7	55°	0	455	−0.2
20090428	70.9	50.5°	−19.2°	459.9	−0.02
20111005	72.4	25.8°	0	405.7	−0.3

[a] Change in Flight Path Angle.

Recall that we use this parameter to control the ray launch direction; ΔFPA = 0 indicates that the source of the signature is the cylindrical Mach-cone of the meteoroid. The computed travel times, column 5 in Table 3, match closely the observed values in Table 2. This is quantified in the last column of Table 3, labeled "% Diff", which reports the percent difference between the computed and the observed values. The largest difference is less than 2% (Meteor 20081028), which is within the ground-intercept radius.

The computed source heights shown in Table 3 are inside the error range reported in Table 2, except for Meteor 20111005. The source height for this case is approximately 1 km below the lower boundary of Silber et al. (2015). Of the two signatures detected for Meteor 20090428, the arrival from the source height of 58.7 km is associated with the cylindrical Mach-cone (ΔFPA = 0), while the later arrival is from a different source (ΔFPA ≠ 0). This interpretation agrees with the ray tracing results of Silber et al. (2015). Similar deviation in the flight path angle is also required for Meteor 20080325. We return to this discussion when we present the pressure signatures of these events in the next section.

5.2. Pressure signatures

Having established the source heights of the signatures, we now compute the nearfield signatures and propagate them to ELFO. Table 4 summarizes the speed, deceleration and remaining mass of each meteoroid at the source height. These are from Silber et al. (2015), who used the fragmentation model of Ceplecha and ReVelle (2005) to fit the observed light curves. The deceleration in all cases is relatively small, so the speed of the meteoroid at the source height is usually within 10% of its entry speed. The ablation effects are more significant, with meteors 20081028 and 20090428 losing almost 30% of their entry mass by the time they reach the source height.

To approximate the physical size of the meteoroid, we assume a spherical shape and use the bulk density estimates from Ceplecha et al. (1998). Table 5 summarizes the diameter of the meteoroid on entry and at the source height. The reduction in the diameter for meteors 20080325 and 20111005 is minor. For meteors 20081028 and 20090428, we simulate both sizes to approximately bound the effects of ablation on the ground signature.

All nearfield simulations are computed in three dimensions, but we take advantage of two-fold symmetry due to the assumed spherical shape. The nearfield signatures are extracted at a distance of 40D. Note that the data from the four ELFO sensors are digitized at a frequency of

Table 4
Trajectory parameters at the source height for each meteor event (Silber et al., 2015).

Date	Speed (km/s)	Deceleration (km/s^2)	Mass (g)
20080325	13.3	0.24	882
20081028	15.0	1.6	77.6
20090428	21.1	0.32	237
20090428	21.2	0.05	330
20111005	28.7	2.3	18.6

Table 5
Meteoroid densities and diameters.

Date	Bulk Density[a] (g/cm^3)	Entry Diameter (cm)	Ablated Diameter (cm)
20080325	3.7	7.8	7.7
20081028	2	4.7	4.2
20090428	2	6.8	6.1
20111005	1	3.4	3.3

[a] Estimated density based on the PE scale of Ceplecha et al. (1998) for small camera data and further adjusted based on orbital parameters.

100 Hz. To compare the measured signatures with the simulations, the measured signatures are filtered with a second-order Butterworth 1 Hz high-pass filter and are then phase aligned. For some of the events, not all sensors were functioning correctly and signatures from those sensors are not shown.

5.2.1. Meteor 20081028

We begin with Meteor 20081028. At the source height $H = 53.7$ km, the freestream Mach number of the meteoroid is 45.6. Fig. 8 shows normalized density contours near the body. Similar to the Stardust validation case (Fig. 4), the flow is dominated by the bow shock. The shock stand-off distance is minuscule – the shock is within 2 mm of the body near the stagnation point and the post-shock density ratio exceeds the perfect gas limit by more than a factor of two.

Fig. 9(a) shows the nearfield signatures extracted at a distance just under one blast radius away for the initial, labeled "D_{INIT}", and ablated, labeled "D_{ABL}", shapes. The overpressure ratios are less than 1, indicating that the signatures are outside the strong-shock regime. The signatures are very similar, with the signature from the smaller ablated shape generating a slightly lower peak and having a slightly shorter duration (earlier zero-crossing) of the positive pressure phase.

Fig. 9(b) shows the computed and observed ground signatures, labeled "ELFO2" and "ELFO4". The agreement is excellent in terms of the shock rise-time, the zero-peak amplitude, the pressure recovery and the period. The duration of the positive pressure phase is under-predicted by approximately 10%. The pressure signature of the ablated

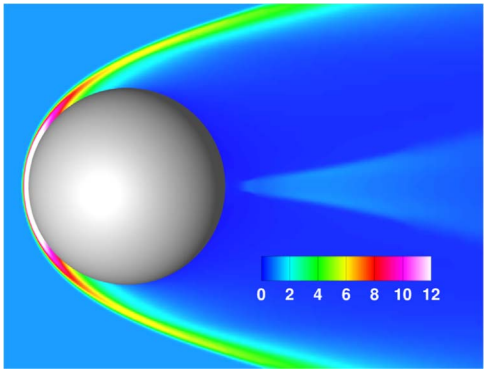

Fig. 8. Contours of normalized density, ρ/ρ_∞, on symmetry plane for Meteor 20081028 ($D = 4.2$ cm, $M_\infty = 45.6$, $H = 53.7$ km).

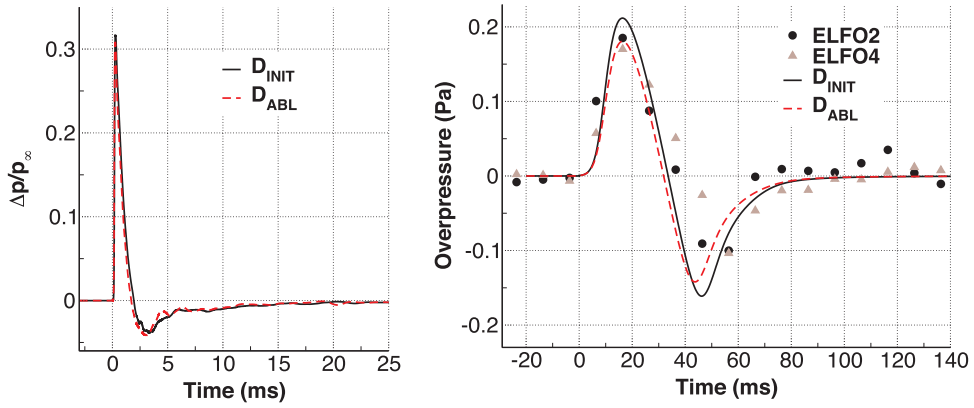

(a) Nearfield pressure signature (b) Ground pressure signature

Fig. 9. Nearfield and ground pressure signatures for Meteor 20081028. Results for the initial and ablated shapes are shown, as well as observations from two ELFO sensors. Nearfield signature extracted at distance of 40D (M_∞ = 45.6 and H=53.7 km).

shape essentially matches the peak amplitude of the observed waveform. The largest deviations are in the slope and depth of the expansion. This is likely caused by uncertainties in the shape of the meteoroid and the atmospheric conditions, as well as the fidelity of the simulation in the wake region of the meteoroid.

The ground signature is a classical N-wave, quite similar to the Stardust signature shown in Fig. 7 except much weaker. This is primarily due to the diameter of the meteoroid being roughly 20 times smaller than that of the capsule. The rounding of the shock discontinuities is much more pronounced in the meteoroid's signature. This stems from the significantly longer propagation distance and the greater height of the source point, which allows the molecular relaxation process to dominate the nonlinear steepening of the signature.

5.2.2. Meteor 20090428

Recall that two arrivals were detected for Meteor 20090428, as summarized in Tables 2 and 3. We start with the first arrival, which is from the cylindrical Mach-cone associated with the ballistic flight of the meteor. The source height is 58.7 km and the freestream Mach number of the meteoroid is 67.5. We simulate both the ablated, D=6.1 cm, and initial, D=6.8 cm, shapes. Fig. 10(a) shows the nearfield signatures for both the ablated and initial shapes, labeled "D_{ABL}" and "D_{INIT}". The overpressure ratios are small and indicate that the shocks are approaching the weakly-nonlinear regime. As expected, the duration of the positive pressure phase of the ablated shape is slightly shorter than that of the initial shape. The small fluctuations visible in the pressure recovery region are from the wake of the meteoroid. They are primarily modeling and numerical artifacts that quickly dissipate as the signature propagates through the atmosphere.

Fig. 10(b) shows the computed signature compared to the ELFO measurements. There is excellent agreement in amplitude of the positive pressure phase. The shock rise time is underpredicted – the main discrepancy is at the foot of the shock where the measurements show an unusually slow ramp up. The measurements also show a wide spread of approximately 30 ms in the duration of the positive pressure phase and there is a factor of two variation in the depth of the expansion. Nevertheless, the computation is within 8% of the observations for two of the four ELFO sensors in terms of positive phase duration and peak-to-peak amplitude. The main difference between the computed and observed signatures is the slope of the trailing recompression. The observed signature takes much longer to recover and contains significant oscillations. This discrepancy most likely stems from our assumption of a single spherical body in the nearfield. This limits the ground signature to a more symmetric waveform than that of the measured signature.

Fig. 11 shows the nearfield and the ground pressure signature of the later arrival from the higher source height H=70.9 km. The signature for only the initial shape is examined because this is sufficiently early in the trajectory where ablation is negligible. The meteoroid's freestream Mach number is 72.1. The overpressure ratio in Fig. 11(a) is slightly higher than that of the first arrival shown in Fig. 10(a) due to the higher Mach number.

Recall that this arrival is not purely from the cylindrical Mach-cone of the meteoroid (see the ray tracing results in Table 3). This is also

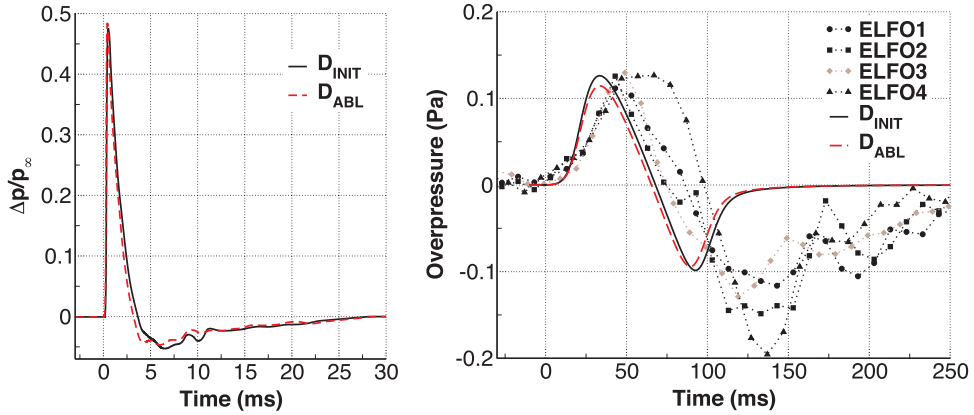

(a) Nearfield pressure signature (b) Ground pressure signature

Fig. 10. Nearfield and ground pressure signatures for the first arrival from Meteor 20090428. Results for the initial and ablated shapes are shown, as well as ELFO observations. Nearfield signature extracted at distance of 40D (M_∞ = 67.5 and H=58.7 km).

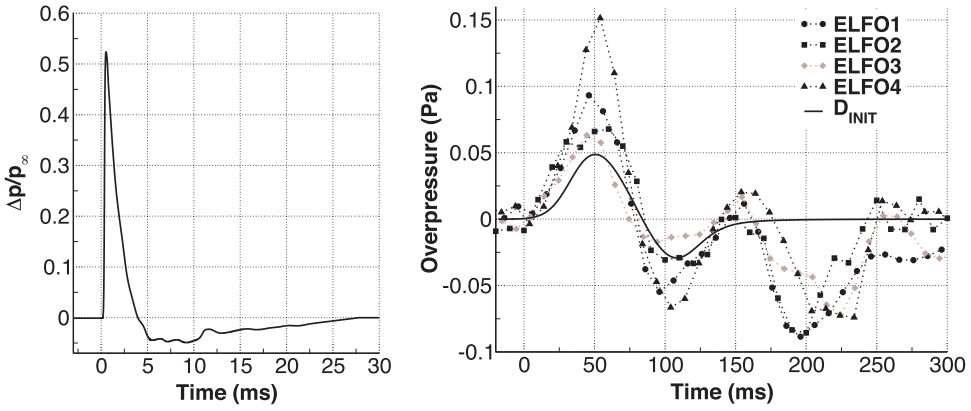

(a) Nearfield pressure signature (b) Ground pressure signature

Fig. 11. Nearfield and ground pressure signatures for the second arrival from Meteor 20090428. Results for the initial (nonablated) shape and ELFO measurements are shown. Nearfield signature extracted at distance of $40D$ ($M_\infty = 72.1$ and $H = 70.9$ km).

supported by the light curve of this event, presented in Silber (2014), which shows an inflection point near this source height that is consistent with high altitude quasi-continuous fragmentation. Despite these circumstances, Fig. 11(b) shows that there is reasonable agreement between the computed and observed signatures. In particular, the duration of the positive pressure phase and the shock rise time agree well. The amplitude is underpredicted by approximately a factor of two. This is reasonable since the simulation does not model energy deposition due to fragmentation. In addition, this analysis helps explain some of the discrepancies noted in the first arrival, since the partial disintegration of the meteoroid at the higher altitude means that the assumption of a spherical shape is most likely inappropriate at the lower altitude.

5.2.3. Meteor 20080325

Meteor 20080325 is the largest ($D \approx 8$ cm) meteoroid of this study. At the source height of 61 km, the freestream Mach number is 42.5. Recall that the ray tracing for this event revealed that the source of the signature is a combination of the Mach cone plus some ablation or fragmentation effects. This is indicated by the large deviation in the ray launch angle shown in Table 3.

Fig. 12 shows the nearfield and the ground pressure signature. The nearfield signature is quite similar to that of Meteor 20081028 shown in Fig. 9(a). Fig. 12(b) shows a significant spread in amplitude measurements among the three sensors. The computed zero-peak amplitude matches one of the sensors well, but underpredicts the other two sensors by almost a factor of 2. The shock rise time is predicted accurately, which suggests that the source-height estimate is correct based on the level of attenuation of the leading shock. The duration of the positive pressure phase is only slightly underpredicted. The simulation, however, misses the trailing part of the waveform, where the measurements show additional compressions and expansions. We attribute this to the simple spherical shape assumed in the nearfield simulation.

5.2.4. Meteor 20111005

The final case features the smallest ($D = 3.4$ cm) and fastest (28.7 km/s) meteoroid of this study. The entry speed corresponds to a freestream Mach number of 98.2 at a source height of 72.4 km. Fig. 13(a) shows the overpressure ratio at a sensor located 1.36 m below the trajectory. Despite the high freestream Mach number, the overpressure ratio remains below unity and hence outside the strong-shock regime. Fig. 13(b) shows the ground signature. While the prediction of the duration of the positive pressure phase and period are reasonable, the amplitude of the computed signature is approximately a factor of 8 too small.

The poor prediction of amplitude is surprising, especially since the ray tracing of this event, summarized in Table 3, indicates that the source of the signature is indeed the cylindrical Mach-cone. A hint of the cause for this discrepancy is the computed source height (72 km), which turned out to be approximately 1 km below the minimum height computed by Silber et al. (2015). Upon re-examination of the light curve for this event, presented in Silber (2014), we find that there is a very pronounced flare near the end of the meteor trail at a height of 72 km. Almost 20% of the original kinetic energy was deposited in this flare over a short height interval. Hence, it is most likely that this

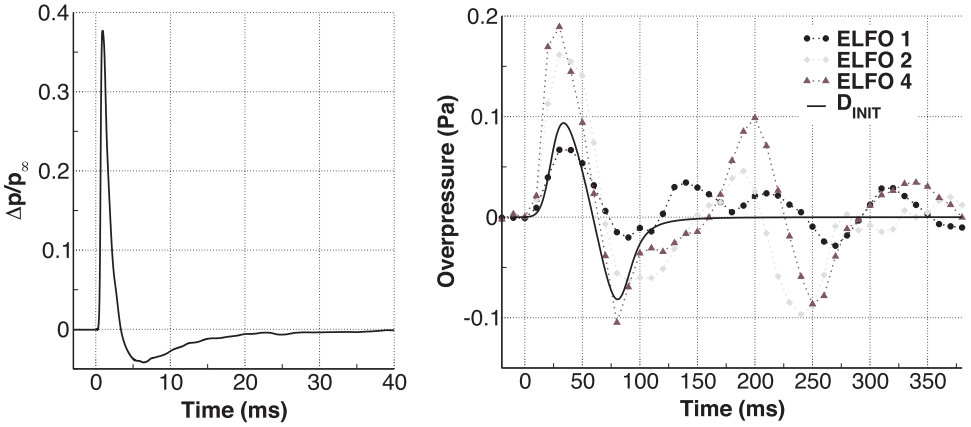

(a) Nearfield pressure signature (b) Ground pressure signature

Fig. 12. Nearfield and ground pressure signatures with ELFO measurements for Meteor 20080325. Nearfield signature extracted at distance of $40D$ ($M_\infty = 42.5$ and $H = 61$ km).

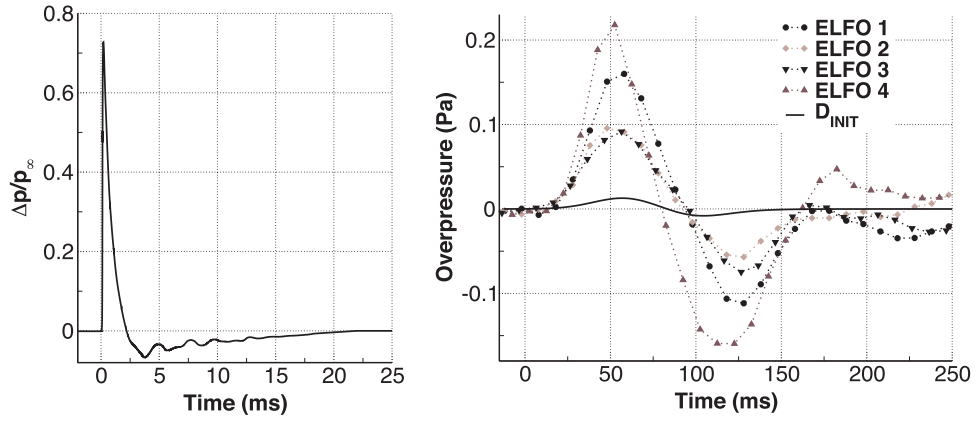

(a) Nearfield pressure signature (b) Ground pressure signature

Fig. 13. Nearfield and ground pressure signatures with ELFO measurements for Meteor 20111005. Nearfield signature extracted at distance of $40D$ ($M_\infty = 98.2$ and $H = 72.4$ km).

signature is dominated by a high-energy spherical source due to the final disintegration of the meteoroid that happens to coincide with a direct ray path.

In hindsight, we should have checked the light curves against our source heights, listed in Table 3, instead of proceeding with the selection based on Table 2. The case is nevertheless instructive, as it demonstrates the importance of non-ballistic sources. Moreover, it also appears to support the findings of Silber et al. (2015) that meteoroid mass estimates are more reliable when based on the signature's period rather than its amplitude.

6. Conclusions

We have demonstrated the first successful validation of a computational approach for predicting meteoric pressure signatures. Overall, the simulations perform remarkably well, considering that the observed signatures are generated by centimeter-sized bodies, and originate from altitudes of at least 50 km and at ranges of about 100 km from the observatory. The approach involves numerically solving the steady, three-dimensional Euler equations to initialize the propagation of a pressure signature through a stratified and windy atmosphere to the ground by using the augmented Burgers' equation. We draw the following conclusions from our results:

- The Stardust entry example establishes a benchmark for the level of accuracy attainable by the simulation under the idealized conditions of a known shape and an energy deposition profile designed to be dominated by drag. This eliminates fragmentation effects and shape uncertainty from affecting the pressure signature and we obtain excellent agreement between the computed and measured signatures.
- For a single N-wave signature, such as Meteor 20081028, the computation matches the morphology of the measured signature extremely well. The period and amplitude of the computed signature are within 1% and 10% of their measured values, respectively, resulting in a sharp estimate of local energy deposition along the meteor trail near the source point.
- More generally, when the source of the signature is predominantly the cylindrical Mach-cone of the ballistic trajectory, the simulation provides an accurate prediction of the leading positive pressure phase of the signature. This includes estimates of the shock rise-time, the zero-peak amplitude and the time to the first zero-crossing of the pressure wave.
- The least accurate result is obtained for Meteor 20111005, where we inadvertently simulate a signature generated by the final disintegration of the meteoroid. Non-ballistic, spherical sources, such as fragmentation, have a strong influence on the signature and these effects would need to be properly modeled to obtain reliable results.
- The computational approach independently verifies the predictions of the Ceplecha and ReVelle (2005) fragmentation model, including its assumptions on luminous efficiency, as well as the density estimates of Ceplecha et al. (1998) for the presented meteor cases.

There are many areas for future work. The use of a computational fluid dynamics solver in the nearfield makes the task of exploring the importance of different shapes and configurations with multiple bodies relatively straightforward. This could potentially improve the prediction of the trailing wave-train, since the single spherical shape used in this study cannot generate multiple compressions and expansions. In addition, the use of solvers appropriate in the transitional flow regime would allow one to lift the 70 km limit on the source height. Roughly half of the 24 signatures analyzed by Silber et al. (2015) have source heights above 75 km, so this is an important area of future work.

Acknowledgements

The authors gratefully acknowledge R. Franz and E. Haering (NASA Armstrong Flight Research Center), and W. Edwards (Natural Resources Canada) for their Stardust pressure signatures. The authors also acknowledge R. Gomez (NASA Johnson Space Center) for providing the surface geometry of the Stardust capsule. This work was supported by the NASA Ames Research Center Contract NNA16BD60C through the Science Mission Directorate's Planetary Defense Coordination Office and the Asteroid Threat Assessment Project. P. Brown was supported by grants from the Natural Sciences and Engineering Research Council of Canada, the Canada Research Chairs Program and NASA co-operative agreement NNX15AC94A. The ELFO infrasound array is funded and operated by Natural Resources Canada.

References

Aftosmis, M.J., Berger, M.J., Melton, J.E., 1998. Robust and efficient Cartesian mesh generation for component-based geometry. AIAA J. 36, 952–960.

Aftosmis, M.J., Berger, M.J., Adomavicius, G., 2000. A Parallel Multilevel Method for Adaptively Refined Cartesian Grids with Embedded Boundaries. AIAA Paper 2000-0808. Reno, NV.

Aftosmis, M.J., Nemec, M., 2014. Cart3D Simulations for the First AIAA Sonic Boom Prediction Workshop. AIAA Paper 2014-0558. http://dx.doi.org/10.2514/6.2014-0558.

Aftosmis, M.J., Nemec, M., Mathias, D.L., Berger, M.J., 2016. Numerical Simulation of Bolide Entry with Ground Footprint Prediction. In: Proceedings of the 54th AIAA Aerospace Sciences Meeting. AIAA Paper 2016-0998, San Diego, CA. http://dx.doi.org/10.2514/6.2016-0998.

Berger, M.J., Aftosmis, M.J., Marshall, D.D., Murman, S.M., 2005a. Performance of a new CFD flow solver using a hybrid programming paradigm. J. Parallel Distrib. Comput. 65, 414–423.

Berger, M.J., Aftosmis, M.J., Murman, S.M., 2005b. Analysis of Slope Limiters on Irregular Grids. AIAA Paper 2005-0490. Reno, NV.

Brown, P.G., Edwards, W.N., ReVelle, D.O., Spurny, P., 2007. Acoustic analysis of shock production by very high-altitude meteors–I: infrasonic observations, dynamics and luminosity. J. Atmos. Sol. -Terr. Phys. 69, 600–620. http://dx.doi.org/10.1016/j.jastp.2006.10.011.

Brown, P.G., ReVelle, D.O., Silber, E.A., Edwards, W.N., Arrowsmith, S., Jackson, L.E., Tancredi, G., Eaton, D., 2008. Analysis of a crater-forming meteorite impact in Peru. J. Geophys. Res. 113. http://dx.doi.org/10.1029/2008JE003105.

Ceplecha, Z., ReVelle, D.O., 2005. Fragmentation model of meteoroid motion, mass loss, and radiation in the atmosphere. Meteorit. Planet. Sci. 40, 35–54. http://dx.doi.org/10.1111/j.1945-5100.2005.tb00363.x.

Ceplecha, Z., Borovička, J., Elford, W.G., ReVelle, D.O., Hawkes, R.L., Porubvcan, V., vSimek, M., 1998. Meteor phenomena and bodies. Space Sci. Rev. 84, 327–471. http://dx.doi.org/10.1023/A:1005069928850.

Cheung, S., Edwards, T., Lawrence, S., 1990. Application of CFD to sonic boom near- and mid-field prediction. In: Proceedings of the 13th AIAA Aeroacoustics Conference. AIAA Paper 90-3999, Tallahassee, FL. http://dx.doi.org/10.2514/6.1990-3999.

Cleveland, R.O., 1995. Propagation of Sonic Booms Through a Real, Stratified Atmosphere (Ph.D. thesis). The University of Texas at Austin.

Desai, P.N., Qualls, G.D., 2008. Stardust Entry Reconstruction. AIAA Paper 2008-1198. Reno, NV.

Edwards, W.N., 2009. Meteor generated infrasound: theory and observation. In: Le Pichon, A., Blanc, E., Hauchecorne, A. (Eds.), Infrasound Monitoring for Atmospheric Studies. Springer, Netherlands, pp. 361–414. http://dx.doi.org/10.1007/978-1-4020-9508-5.

Edwards, W.N., Brown, P.G., Weryk, R.J., ReVelle, D.O., 2008. Infrasonic observations of meteoroids: preliminary results from a coordinated optical-radar-infrasound observing campaign. Earth Moon Planets 102, 221–229. http://dx.doi.org/10.1007/s11038-007-9154-6.

Evers, L.G., Haak, H.W., 2001. Listening to sounds from an exploding meteor and oceanic waves. Geophys. Res. Lett. 28, 41–44. http://dx.doi.org/10.1029/2000GL011859.

Few, A.A., 1969. Power spectrum of thunder. J. Geophys. Res. 74, 6926–6934. http://dx.doi.org/10.1029/JC074i028p06926.

Haering, E.A., Murray, J.E., Purifoy, D.D., Graham, D.H., Meredith, K.B., Ashburn, C.E., Stucky, M., 2005. Airborne shaped sonic boom demonstration with computational fluid dynamics comparisons. In: Proceedings of the 43rd AIAA Aerospace Sciences Meeting and Exhibit. AIAA Paper 2005-0009, Reno, NV.

Haynes, C.P., Millet, C., 2013. A sensitivity analysis of meteoric infrasound. J. Geophys. Res. Planets 118, 2073–2082. http://dx.doi.org/10.1002/jgre.20116.

Hedin, A., Fleming, E., Manson, A., Schmidlin, F., Avery, S., Clark, R., Franke, S., Fraser, G., Tsuda, T., Vial, F., Vincent, R., 1996. Empirical wind model for the upper, middle and lower atmosphere. J. Atmos. Terr. Phys. 58, 1421–1447. http://dx.doi.org/10.1016/0021-9169(95)00122-0.

Henneton, M., Gainville, O., Coulouvrat, F., 2015. Numerical simulation of sonic boom from hypersonic meteoroids. AIAA J. 53, 2560–2570.

Jones, D.L., Goyer, G.G., Plooster, M.N., 1968. Shock wave from a lightning discharge. J. Geophys. Res. 73, 3121–3127. http://dx.doi.org/10.1029/JB073i010p03121.

Le Pichon, A., Antier, K., Cansi, Y., Hernandez, B., Minaya, E., Burgoa, B., Drob, D., Evers, L.G., Vaubaillon, J., 2008. Evidence for a meteoritic origin of the September 15, 2007, Carancas crater. Meteorit. Planet. Sci. 43, 1797–1809. http://dx.doi.org/10.1111/j.1945-5100.2008.tb00644.x.

Liszka, L., 2008. Listening to Meteors: Infrasonic Observations of Meteors in Northern Sweden. Scientific Report 295. Swedish Institute of Space Physics. SE-981 28 Kiruna, Sweden.

Maglieri, D.J., Bobbitt, P.J., Plotkin, K.J., Shepherd, K.P., Coen, P.G., Richwine, D.M., 2014. Sonic Boom: Six Decades of Research. NASA/SP-2014-622. ⟨http://hdl.handle.net/2060/20150006843, visited September 2016.

Millet, C., Haynes, C.P., 2010. Stochastic Model Approach of Meteor-Generated Infrasound. AIAA Paper 2010-7999. Toronto, ON.

Nemec, M., Aftosmis, M.J., 2014. Toward Automatic Verification of Goal-Oriented Flow Simulations. NASA/TM 2014-218386. National Aeronautics and Space Administration. Center for AeroSpace Information, 7115 Standard Drive, Hanover, MD 21076. ⟨http://hdl.handle.net/2060/20150000864⟩.

Page, J.A., Plotkin, K.J., 1991. An efficient method for incorporating computational fluid dynamics into sonic boom prediction. In: Proceedings of the 9th AIAA Applied Aerodynamics Conference. AIAA Paper 91-3275, Baltimore, MD.

Park, M.A., Morgenstern, J.M., 2016. Summary and statistical analysis of the first AIAA sonic boom prediction workshop. J. Aircr. 53, 578–598. http://dx.doi.org/10.2514/1.C033449.

Park, M.A., Aftosmis, M.J., Campbell, R.L., Carter, M.B., Cliff, S.E., Bangert, L.S., 2013. Summary of the 2008 NASA Fundamental Aeronautics Program Sonic Boom Prediction Workshop. AIAA Paper 2013–0649. Grapevine, TX. (51st AIAA Aerospace Sciences Meeting). http://dx.doi.org/10.2514/6.2013-649.

Picone, J.M., Hedin, A.E., Drob, D.P., Aikin, A.C., 2002. NRLMSISE-00 empirical model of the atmosphere: statistical comparisons and scientific issues. J. Geophys. Res. 107. http://dx.doi.org/10.1029/2002JA009430.

Plotkin, K., Franz, R.J., Haering, E.A., 2006. Prediction and measurement of a weak sonic boom from an entry vehicle. Paper 2aPA3. In: Proceedings of the Fourth Joint Meeting of the Acoustical Society of America and the Acoustical Society of Japan. Wyle Laboratories and NASA Dryden Flight Research Center.

Rallabhandi, S.K., 2011. Advanced sonic boom prediction using the augmented burgers equation. J. Aircr. 48, 1245–1253. http://dx.doi.org/10.2514/1.C031248.

Revelle, D.O., Edwards, W.N., 2007. Stardust–an artificial, low-velocity meteor" fall and recovery: 15 January 2006. Meteorit. Planet. Sci. 42, 271–299. http://dx.doi.org/10.1111/j.1945-5100.2007.tb00232.x.

ReVelle, D.O., 1976. On meteor-generated infrasound. J. Geophys. Res. 81, 1217–1230. http://dx.doi.org/10.1029/JA081i007p01217.

ReVelle, D.O., Whitaker, R.W., 1999. Infrasonic detection of a Leonid bolide: 1998 November 17. Meteorit. Planet. Sci. 34, 995–1005. http://dx.doi.org/10.1111/j.1945-5100.1999.tb01419.x.

ReVelle, D.O., 1974. Acoustics of Meteors – Effects of the Atmospheric Temperature and Wind Structure on the Sounds Produced by Meteors (Ph.D. thesis). University of Michigan.

Siclari, M., Darden, C., 1991. CFD predictions of the near-field sonic boom environment for two low boom HSCT configurations. In: Proceedings of the 22nd AIAA Fluid Dynamics, Plasma Dynamics & Lasers Conference. AIAA Paper 91-1631, Honolulu, HI.

Silber, E.A., Brown, P.G., 2014. Optical observations of meteors generating infrasound–I: acoustic signal identification and phenomenology. J. Atmos. Sol. -Terr. Phys. 119, 116–128. http://dx.doi.org/10.1016/j.jastp.2014.07.005.

Silber, E.A., Brown, P.G., Krzeminski, Z., 2015. Optical observations of meteors generating infrasound: weak shock theory and validation. J. Geophys. Res. Planets 120, 413–428. http://dx.doi.org/10.1002/2014JE004680.

Silber, E.A., 2014. Observational and Theoretical Investigations of Cylindrical Line Source Blast Theory Using Meteors (Ph.D. thesis). University of Western Ontario.

Srinivasan, S., Tannehill, J.C., Weilmuenster, K.J., 1987. Simplified Curve Fits for the Thermodynamic Properties of Equilibrium Air. NASA Reference Publication 1181. National Aeronautics and Space Administration.

Stackpoole, M., Sepka, S., Cozmuta, I., Kontinos, D., 2008. Post-Flight Evaluation of Stardust Sample Return Capsule Forebody Heatshield Material. AIAA Paper 2008-1202. Toronto, ON. http://dx.doi.org/10.2514/6.2008-1202.

Sutherland, L.C., Bass, H.E., 2004. Atmospheric absorption in the atmosphere up to 160 km. J. Acoust. Soc. Am. 115, 1012–1032. http://dx.doi.org/10.1121/1.1631937.

Swinbank, R., O'Neill, A., 1994. A stratosphere-troposphere data assimilation system. Mon. Weather Rev. 122, 686–702. http://dx.doi.org/10.1175/1520-0493(1994)1222.0.CO;2.

Trumble, K.A., Cozmuta, I., Sepka, S., Jenniskens, P., Winter, M., 2010. Postflight aerothermal analysis of Stardust sample return capsule. J. Spacecr. Rockets 47, 765–774. http://dx.doi.org/10.2514/1.41514.

Tsikulin, M.A., 1970. Shock Waves During the Movement of Large Meteorites in the Atmosphere. Technical Report. English Translation AD 715-537. Naval Intelligence Command. Alexandria, VA.

U.S. Standard Atmosphere, 1976. National Oceanic and Atmospheric Administration, National Aeronautics and Space Administration, and the U.S. Air Force, U.S. Government Printing Office, Washington D.C.

Weryk, R.J., Brown, P.G., Domokos, A., Edwards, W.N., Krzeminski, Z., Nudds, S.H., Welch, D.L., 2008. The Southern ontario all-sky meteor camera network. Earth Moon Planets 102, 241–246. http://dx.doi.org/10.1007/s11038-007-9183-1.

Whipple, F.J.W., 1923. Determination of the temperature of the upper atmosphere by meteor observations. Nature 112, 759. http://dx.doi.org/10.1038/112759a0.

Whitham, G.B., 1956. On the propagation of weak shock waves. J. Fluid Mech. 1, 290–318. http://dx.doi.org/10.1017/S0022112056000172.

Wintzer, M., Ordaz, I., Fenbert, J.W., 2015. Under-track CFD-based shape optimization for a low-boom demonstrator concept, In: Proceedings of the 33rd AIAA Applied Aerodynamics Conference. AIAA Paper 2015-2260, Dallas, TX.

Yamamoto, M., Hashimoto, A., Aoyama, T., Sakai, T., 2015. A unified approach to an augmented Burgers equation for the propagation of sonic booms. J. Acoust. Soc. Am. 137, 1857–1866. http://dx.doi.org/10.1121/1.4916833.